Ejecta Behavior during Plume-Surface Interactions under Rarefied Atmospheric Conditions

Lokesh Silwal[a], Vikas N. Bhargav[a], Daniel C. Stubbs[a], Brandon K. Fulone[a], Brian S. Thurow[a], David E. Scarborough[a], Vrishank Raghav[a,b]

[a]*Department of Aerospace Engineering, Auburn University, Davis Hall, Auburn, 36849, AL, USA*
[b]*Corresponding author (raghav@auburn.edu)*

Abstract

Plume-surface interactions (PSI) occur during the take-off and landing of interplanetary vehicles, leading to particle ejection and the formation of craters. This can be detrimental to the vehicle and any structures or infrastructure near the landing site. A major challenge in developing a comprehensive understanding of this three-dimensional phenomenon is the need to characterize the ejecta and cratering dynamics simultaneously. Here, experiments are conducted in a vacuum chamber at different nozzle heights and ambient pressure conditions using high-speed stereo-photogrammetry and planar particle tracking velocimetry to quantify the cratering and ejecta dynamics. Predictably, it was observed that the trajectory of ejecta with a large Stokes number was mostly unaffected by the nozzle flow after leaving the crater. Under rarefied conditions, the ejecta kinematics (velocity, ejection angle, range, and height) were significantly different compared to continuum conditions. Finally, the findings demonstrate a dependency between ejecta kinematics and crater topology for the current test cases, providing critical insights into particle ejection's initial characteristics.

Access paper on journal website - Click here

Keywords: Ejecta kinematics, Crater dynamics, stereo photogrammetry, particle tracking velocimetry, entry descent and landing, Retropropulsion

1. Introduction

Understanding Plume-Surface Interactions (PSI), which is the interaction between a rocket's exhaust plume and the planetary surface, is crucial for the safe return of humans to the moon, the deployment of scientific instruments on celestial bodies, and Mars exploration. Depending on the makeup of the planet's surface, PSI usually results in the formation of craters and high-velocity ejected particles (referred to as ejecta) that risk damaging landers or nearby instruments. The risks of contamination and damage associated with PSI were first observed during Apollo missions, where dust clouds generated during lunar landings caused visibility issues and damage to onboard tracking sensors, as documented in studies such as [1]. Other examples of impacts from PSI include surface pitting on the Surveyor III craft during Apollo 12 [2] and the tilted landing of the Apollo 15 lander due to ejecta cloud obstruction, as shown in Fig. 1. Astronauts, including John Young and Gene Cernan, regarded lunar dust as one of the most significant obstacles to returning to and operating on the Moon [1, 3, 4]. As such, PSI is recognized as a critical challenge for the Artemis program, which will involve landers operating at high thrust levels and near lunar outposts where damage to existing equipment is possible.

During the Apollo era, valuable insights into PSI were gained from images captured during landings. Several studies have reported the potential impact of the high-speed ejecta on the surrounding structures when landing on lunar conditions by examining the impact on the Surveyor 3 [2, 5]. The effects of PSI under rarefied conditions such as in the lunar environment have also been documented in the literature [6, 7]. In addition, terrestrial studies conducted in the latter half of the twentieth century contributed to our understanding of PSI. Roberts in the 1960s [8, 9, 10, 11] identified viscous erosion, which is a mechanism of crater formation where shear stresses between the jet and the

granular surface cause the ejecta to move radially away from the center of the plume, as one of the primary mechanisms of the crater formation process.

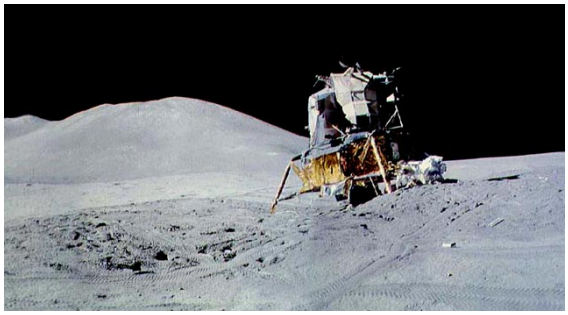

Figure 1: Apollo 15 lander module situated precipitously on the edge of the lunar crater after touchdown due to obscured visibility from the ejecta [12].

Subsequent studies tested Roberts' theory and identified additional cratering mechanisms like bearing capacity failure and diffused gas eruption. Hutton [13] conducted laboratory-scale experiments to validate the predictions of Roberts theory under lunar atmospheric conditions and suggested further experiments to improve its accuracy. Alexander [14] proposed the concept of bearing load capacity failure, where the pressure beneath the jet exceeds the bearing capacity of the soil, causing the soil to be pushed downward and outward and forming a nearly cylindrical crater. Scott and Ko [15] observed diffused gas eruption as another cratering mechanism. In this mechanism, the radial diffusion of propellant gas into the regolith leads to gas pressure gradients in the regolith that can lift the overlying soil.

Another recently discovered mechanism is diffuson-driven flow. Depending on the permeability of the regolith, some flow penetrates the surface, resulting in a pressure gradient between the surface of the regolith and locations deeper within the regolith, resulting in gas flow through the regolith bed and away from the location of the primary plume impingement. This flow imparts a drag force on sub-surface regolith particles. Sub-surface particles are carried along with the gas if this drag force exceeds the cohesive forces [16, 17].

The recent focus on PSI research, driven by NASA's Artemis program, has resulted in increased numerical and experimental studies into the physics of PSI. Most experimental studies have been conducted using half-domain experiments, which utilize a transparent splitter plate aligned with the symmetry plane of the nozzle flow. This physical arrangement allows for optical access to a cross-section of the crater, enabling detailed observation of the plume-surface interaction [18, 19, 17, 20, 21, 22, 23]. These experiments investigated the effects of parameters that include physical properties of regolith simulant [18], nozzle height and descent rate [18], jet velocity and density [24, 17], gravity conditions [20], and ambient pressure conditions [25]. However, these studies focused on characterizing the cratering dynamics with limited attention given to studying the behavior of ejecta across a wide range of parameters.

Predicting ejecta behavior has been primarily based on numerical analysis, but validating these models is challenging because of the difficulties in measuring and extracting relevant ejecta properties under reduced ambient and gravity conditions. Properties of interest include the initial ejection conditions, such as velocities, angles, location relative to the crater, and the trajectories followed by the ejecta. The physics of the problem indicates that the jet momentum and crater properties influence the initial conditions of the ejection. However, a comprehensive study that establishes the influence of these factors on ejecta kinematics is lacking. Accurately studying the physics of this problem is crucial for estimating properties such as the maximum vertical and horizontal extent traveled by the ejecta, which is important for assessing the potential damage to landers and surrounding structures. Understanding the physics of the problem can also help augment the predictive capabilities of the predictive tools currently being developed to model the properties of ejecta.

A fundamental understanding of this problem can be gained through scaled-down experiments under relevant conditions, but even these experiments have their own associated challenges. Due to the high density of ejecta, measurements of the crater and ejecta properties near the crater rim become challenging. Additionally, obtaining complete ejecta trajectories is difficult, as conducting experiments under rarefied atmospheres requires a large physical space. Despite these challenges, extracting properties of interest from the limited ejecta measurements using simple

ballistic models can aid in understanding the ejecta behavior under different operating conditions. However, the ejecta can also be affected by the high-speed jet flow deflected off the crater, which could deviate the ejecta path from its ballistic path. Comparing measured ejecta trajectories with the ballistic trajectory can help quantify the influence of nozzle flow.

This study uses optical diagnostic techniques [26, 27, 28, 29] to address some of these challenges and outstanding scientific questions through simultaneous cratering dynamics and ejecta kinematics measurements during PSI. Stereo-photogrammetry was used to quantify cratering dynamics, and planar particle tracking velocimetry was used to measure ejecta kinematics. Experiments were carried out in a vacuum chamber for different nozzle heights ($h/D = 55.6, 37.1, 23.2, 9.3$) and ambient pressure conditions (101.3 kPa and 0.033 kPa) using a regolith simulant bed with particle diameters ranging $600\mu m \leq d_p \leq 850\mu m$. The measured ejecta tracks were compared with the ballistic tracks to determine whether the nozzle flow influenced the ejecta properties and if a ballistic model could be used to extract relevant ejecta properties. The influence of nozzle height and ambient pressure conditions on ejecta kinematics was then explored. Finally, the relationship between crater topology, which includes the crater rim and ramp angle, and the location, velocity, and angle of initial ejection of the ejecta were studied.

2. Methods

Experimental Facility

The current study employed the experimental setup shown in Fig. 2a, a custom-designed vacuum chamber with dimensions of 1.2 m in length, width, and height. The chamber had 0.45 m square windows on its front, left, right, and top surfaces for optical access. The top window provided access to a pair of cameras and associated lighting to perform 3-D measurements of the crater geometry using stereo-photogrammetry. The front and side windows were used for illumination and image acquisition for planar particle tracking velocimetry. A schematic of the simultaneous measurement of stereo photogrammetry and particle tracking is shown in Fig. 3. High-speed stereo image pairs were obtained at a frame rate of $1,000$ Hz using two Phantom VEO640L cameras with a resolution of 2560×1600 px. The stereo image pair was then used to quantify the depth of surface features [30, 31]. Further details on the stereo photogrammetry technique are reported by Stubbs et al. [27, 32].

The ejecta measurements were made in a plane that passed through the nozzle axis and was perpendicular to the undisturbed sand bed. Particle illumination in this plane was achieved using a high-power continuous laser. The laser beam was converted to a planar sheet through a cylindrical lens. Images of the illuminated region were captured using a Phantom VEO4K 990L high-speed camera at a frame rate of 2 kHz and 4 kHz for the continuum and rarefied cases, respectively. The latter case was acquired at a higher frame rate because the ejecta were seen to travel faster compared to continuum conditions. Due to limitations in the camera acquisition rate, the cameras operated at a resolution of 2048×1024 px and 2048×520 px for the continuum and rarefied cases, respectively.

To ensure that the stereo lighting did not interfere with ejecta measurements, the exposure timing of the two cameras and the LED lights had to be carefully controlled. This was accomplished by delaying the start of the frame exposure for the stereo cameras by the exposure time of the ejecta camera of 50 μs so that the stereo camera frame exposure began only after the ejecta camera frame exposure was complete. The exposure time of the stereo cameras was also limited to a value of 200 μs so that the exposure of the stereo camera was completed before the next exposure of the ejecta camera frame started. Fig. 2b shows the timing diagram for the exposure of the two types of cameras. The acquisition rate for the stereo cameras was fixed at 1000 Hz, while the ejecta measurements were taken at 2000 Hz and 4000 Hz for continuum and rarefied conditions, respectively. This setup allowed for the acquisition of one stereo image and two ejecta images per frame for continuum conditions and four ejecta images per frame for rarefied conditions, as shown in Fig. 2b.

Instrumentation

The vacuum chamber had electrical pass-throughs for remote control of the nozzle height and measurement of the static pressure and temperature of the nozzle. The chamber also had a pass-through to provide compressed air to the nozzle. The system was remotely controlled using a National Instruments (NI) compact data acquisition system (cDAQ-9189). It contained an NI 9482 relay module for triggering cameras and solenoid valve, an NI 9474 digital output module for controlling the stepper motor, an NI 9401 TTL module for providing synchronization pulses to the

stereo and ejecta cameras, an NI 9217 module for measuring the nozzle temperature, and an NI 9222 analog voltage input module for measuring the nozzle pressure transducer, mass flow meter, and solenoid trigger voltage. The static pressure and the temperature at the nozzle inlet were monitored using an Endevco 8530BM37-200-1 pressure transducer and Omega PR-11-2-100-1/16-4-E RTD temperature probe, respectively. An Omega FMA5545 mass flow meter was located upstream of the nozzle solenoid valve to measure the mass flow rate through the nozzle. The chamber pressure was also monitored using an InstruTech GVG101 Convection Gauge mounted to the front top left corner of the chamber. Compressed air was passed through a stainless steel tube with a constant inner diameter of 4.93 mm to generate an under-expanded choked flow with Mach number 1 at the nozzle exit. A solenoid valve upstream of the nozzle was used to remotely control the initiation and termination of nozzle flow.

Quantification of particle size distribution

The nozzle jet impinged on a simulant bed of sand particles with diameters ranging from d_p = 600 to 850 μm. Image analysis of random samples of sand particles was used to quantify the particle size distribution. Images were taken using a Nikon Z50 camera with a 60mm macro lens with uniform illumination achieved using four LED lights. A total of 11,000 particles were considered to ensure statistically significant quantification of the particle size distribution. After image acquisition, FIJI software was used to process the images and measure the particle size distribution [33]. A sample of the raw image and the measured particle size distribution are shown in Fig. 2c. The sand was near-cohesion-less, nearly pure quartz, and conformed to the American Society for Testing and Materials (ASTM) C 778 standard with a reported particle density of ρ_p = 2650 kg/m^3. The bulk density of the sand bed was determined to be 1650 kg/m^3, indicating a packing ratio of 0.6. Additional details of the facility are reported by Stubbs [32].

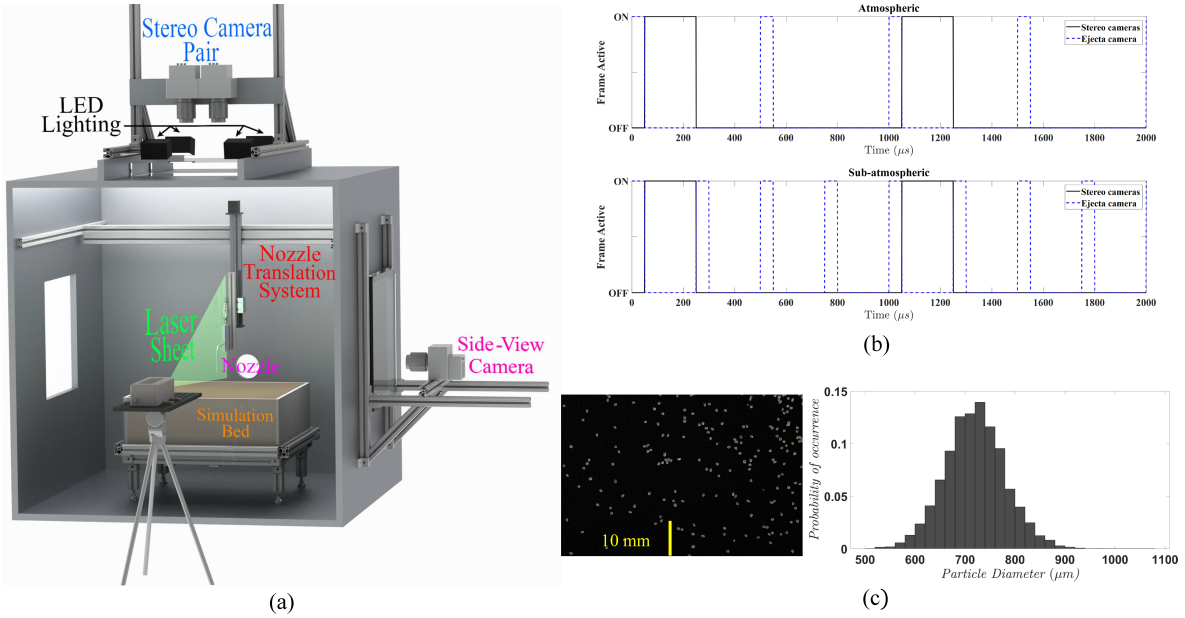

Figure 2: (a) Schematic of the rarefied PSI experimental setup, (b) camera timing diagrams to facilitate simultaneous crater and ejecta measurements under continuum and rarefied conditions; ON state refers to the time duration when camera sensors are exposed, (c) sample of the raw images taken to quantify the particle size distribution, and particle size distribution obtained after post-processing the raw images using FIJI software.

Operating conditions

The experiments were conducted at nozzle heights ranging from h/D = 55.6 to h/D = 9.3 at ambient chamber pressures of 101.3 kPa and 0.033 kPa. Each of these measurements was repeated three times to quantify the statistical significance of the results. The summary of the parameters is listed in Table 1. For each condition, the nozzle operated for two seconds with a measured static pressure and mass flow rate of 305 kPa and 8.5 g/s, respectively.

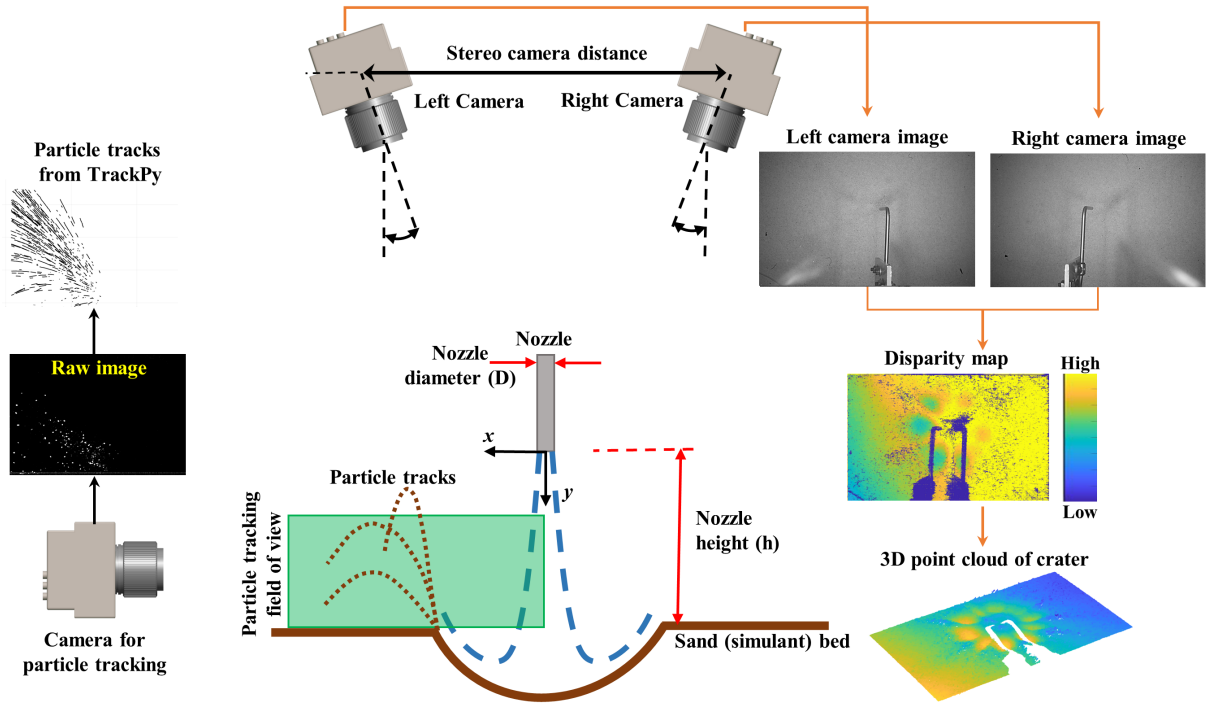

Figure 3: Diagram depicting the measurement of crater geometry using stereo-photogrammetry technique and ejecta dynamics using the particle tracking velocimetry technique.

Table 1: Summary of the parametric space for the current study

Ambient pressure	Ejecta camera	Stereo cameras	Nozzle heights (h/D)
101.3 kPa	2000 Hz, (2048x1024) pixels	1000 Hz, (2560x1600) pixels	55.6, 37.1, 23.2, 9.3
0.033 kPa	4000 Hz, (2048x520) pixels		

Particle tracking

A two-dimensional particle tracking technique was used to measure ejecta kinematics. The light reflected by the ejecta particles in the illuminated region of interest was captured using a high-speed camera. The acquired images were processed using the open-source software Trackpy [34]. This software first processed the images to identify all the particles in each frame based on a user-defined intensity threshold. Next, these particles were tracked over subsequent frames based on a user-defined interrogation window concerning each particle. Finally, the displacements of these particles over successive frames were calculated. This study used an interrogation window size of 25×25 px. Ultimately, this resulted in a data set containing the spatial positions and displacements in pixel coordinates for all detected particles. These data were transformed to physical coordinates and further analyzed to characterize ejecta kinematics. Note that the camera acquisition frame rate and the interrogation window size defined above were carefully chosen to identify particle tracks while ensuring that the process is computationally efficient and that the particle displacements within the interrogation windows were fully captured without getting truncated.

Data post-processing

Crater ramp angle measurement: The stereo photogrammetry technique produces a point cloud representation of the full three-dimensional crater shape. These data are further processed to extract the desired geometric properties of the crater, such as the crater wall angle and radius. The approach to extracting the radius of the crater has been explained by Stubbs [27, 32]. The extraction of the crater wall angle was performed as follows. First, the crater geometry was sliced along the XY plane centered on the nozzle axis. Then, a parabola was fit only through the points

deeper than 2 *mm* to avoid including surface points in the fit since they are of poor quality. The crater wall angle was then calculated as the first derivative of the fitted parabolic function evaluated at the surface.

Ejecta kinematics: To study the ejecta kinematics, the ballistic model was used to obtain the velocity and ejection angle at the undisturbed sand surface and the range and maximum height achieved by ejecta. The process for analyzing the ejecta trajectories using the ballistic model is shown in Fig. 7 and is explained below. First, the tracks of all the identified ejecta from TrackPy were extracted. Next, their kinematics (velocity and trajectory angle) from the initial time point of the extracted tracks were used as input to the ballistic model to generate ballistic tracks. The Root Mean Square Error (RMSE) between the actual and ballistic tracks was then calculated, which is given as follows:

$$RMSE = \sqrt{\int_{t_1}^{t_2} \left(\sqrt{(x^2 + y^2)_{ballistic}} - \sqrt{(x^2 + y^2)_{experiments}} \right)^2 dt} \tag{1}$$

The RMSE quantifies the average deviation between the experimental and the corresponding ballistic tracks over the duration the experimental tracks were obtained, i.e., $t_1 - t_2$ (Fig. 7).

The ballistic model was then used to regress in time and project the ejecta properties to obtain the velocity and ejection angle at the undisturbed sand surface (see Fig. 7). Similarly, the projection was performed forwards in time to obtain the range and maximum height achieved by ejecta. The analysis was performed for all the particles that were visible in a given frame and moving radially outward. The values of ejecta velocity $|V|$, ejection angle α, ejecta trajectory range R, and ejecta trajectory height H were obtained for all the particles originating from the undisturbed sand bed at a time instant t. Then each of these properties was averaged for all the ejecta originating at the undisturbed sand bed over a temporal bin size of $5ms$. The bin size was optimally chosen to average out the noise while also making sure to avoid the loss of dynamic features due to averaging. The evolution of these averaged parameters is plotted and compared across continuum and rarefied conditions in Fig. 9. The variance of these results over three repetitions under the same condition was also analyzed.

Next, while correlating the ejecta kinematics with the crater properties, certain considerations were made to characterize the crater geometry. Since the variation in the crater radius between the initial sand surface and a depth of 2 *mm* is expected to be minimal, all crater radius values were calculated only after the depth breaches 2 *mm*. This method provides a reliable estimate of the location of the crater rim. The detailed methodology for calculating the crater radius has been reported by Stubbs et al. [27].

Statistical analysis

Primarily, two correlations were investigated in the present study. First, the correlation between the crater rim and the location of the ejection from the undisturbed sand bed. Second, the correlation between the crater ramp angle and ejection angle. These correlations were carried out only for rarefied conditions, as the duration for which the crater geometry could be successfully measured was insufficient under continuum conditions. The correlation analysis between the crater rim and the ejection location has been analyzed by calculating the residuals (r_i) between the crater rim location (R_C) and the projected ejection location (R_P). The residuals here are given as follows:

$$r_i = R_C - R_P \tag{2}$$

Table 2 provides a summary of the temporal range used to calculate these residuals. Similarly, a linear regression model was used to quantify the correlation between the crater ramp angle and the ejecta angle. Here, the crater ramp angle (θ_c) was taken as the independent variable with the ejecta angle (θ_e) as a dependent variable. The regression model is given as follows:

$$\theta_e = m\theta_c + c \tag{3}$$

Where m is the slope and c is the intercept. The linear model was developed using samples spaced 50 ms apart for one of the measurement cases (out of the three) at each nozzle height. Bartlett's test was used to test the normality and equal variance criteria for the samples at a significance level of 0.05. Similarly, the one-way Analysis of Variance (ANOVA) test was used to determine whether the sample means differed significantly for every 50 ms at a significance level of 0.05. The starting time point was chosen to ensure that the crater radius growth had reached a

quasi-steady state, as previously reported by Stubbs et al. [27, 32]. The analysis was then calculated up to the point where the quality of the crater reconstruction was insufficient to extract the crater ramp angle.

3. Results

General crater and ejecta behavior

Parameters such as nozzle heights and ambient pressure modify the jet structure that impinges on the granular bed, ultimately affecting the dynamics of the crater during PSI. Schlieren was carried out to visualize the effects of these parameters on the jet structure. Fig 4 shows the jet flow features at the ambient pressure conditions of $101.3kPa$ and $0.033kPa$, respectively. The images show that the jet is highly under-expanded under low ambient pressure conditions. Consequently, the interaction area between the jet and the granular bed increases when the ambient pressure is reduced. This results in the formation of a much wider and shallower crater under rarefied conditions compared to the continuum case. The effects of nozzle height are also apparent in the flow visualization for the continuum case. As the distance below the nozzle exit increases, the flow becomes more diffused due to viscosity, and the jet area increases. As a result, the impingement area on the simulant bed increases with increasing nozzle height. Thus, the craters are expected to be wider and shallower, with smaller crater ramp angles for higher nozzle heights.

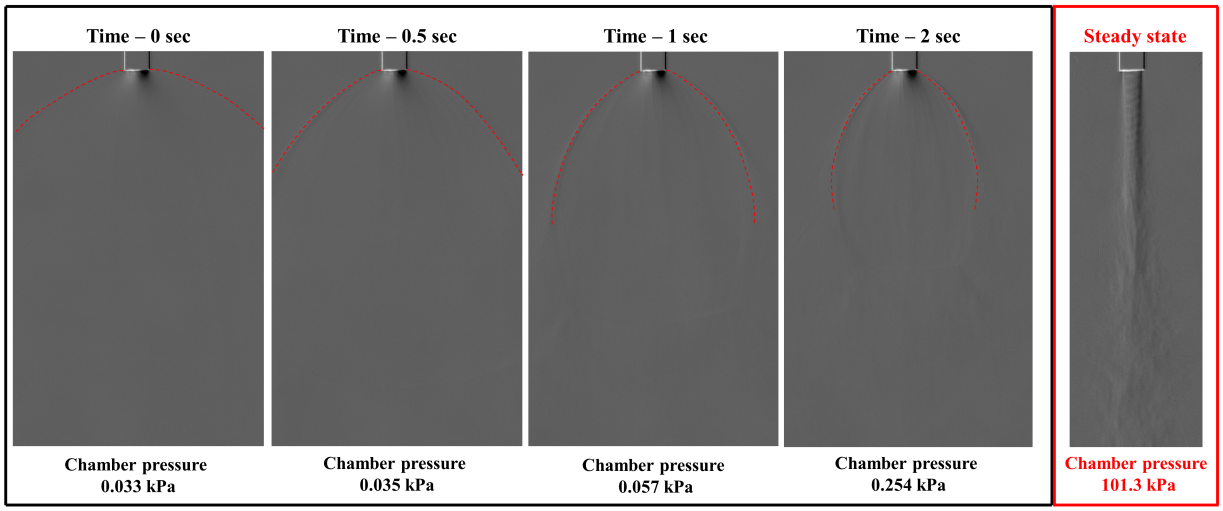

Figure 4: Qualitative visualization of the nozzle flowfield using Schlieren. Dashed red lines are drawn to highlight the variation in jet contraction during the test duration.

To confirm this, the crater shape at the central plane was extracted from the point cloud, and some example cases for specific nozzle heights and ambient pressure conditions are plotted in Fig 5. The results show that the crater shape remains parabolic for the continuum case. These results are on par with the observations made by Stubbs [27]. The crater gets deeper with steeper walls as the nozzle height is reduced. In contrast to the continuum pressure cases, the crater does not exhibit a parabolic shape for rarified ambient conditions. Rather, for rarefied conditions, the deepest point in the crater is formed at locations farther away from the crater center. This is a classic example of crater formation due to the viscous erosion process, as discussed by Roberts.

Robert's theory predicts that during the viscous erosion process, the deepest point of the crater forms at a location away from the crater, which also corresponds to the location of the maximum dynamic pressure. The crater's center corresponds to the stagnation region with minimal erosion. The observed formation of a hump at the crater center and the fact that the location of the maximum depth is at some distance radially away from the crater center under rarefied conditions point to the fact that the cratering mechanisms under rarefied conditions are dominated by viscous erosion.

Under rarefied conditions, the crater also exhibited a "lobed" crater shape for nozzle heights greater than 9.3D. These structures are illustrated in Fig. 6 and are characterized by azimuthal depth variations wherein peaks corresponded with locations of ejecta streaks and valleys that existed between them. This type of structure has also been

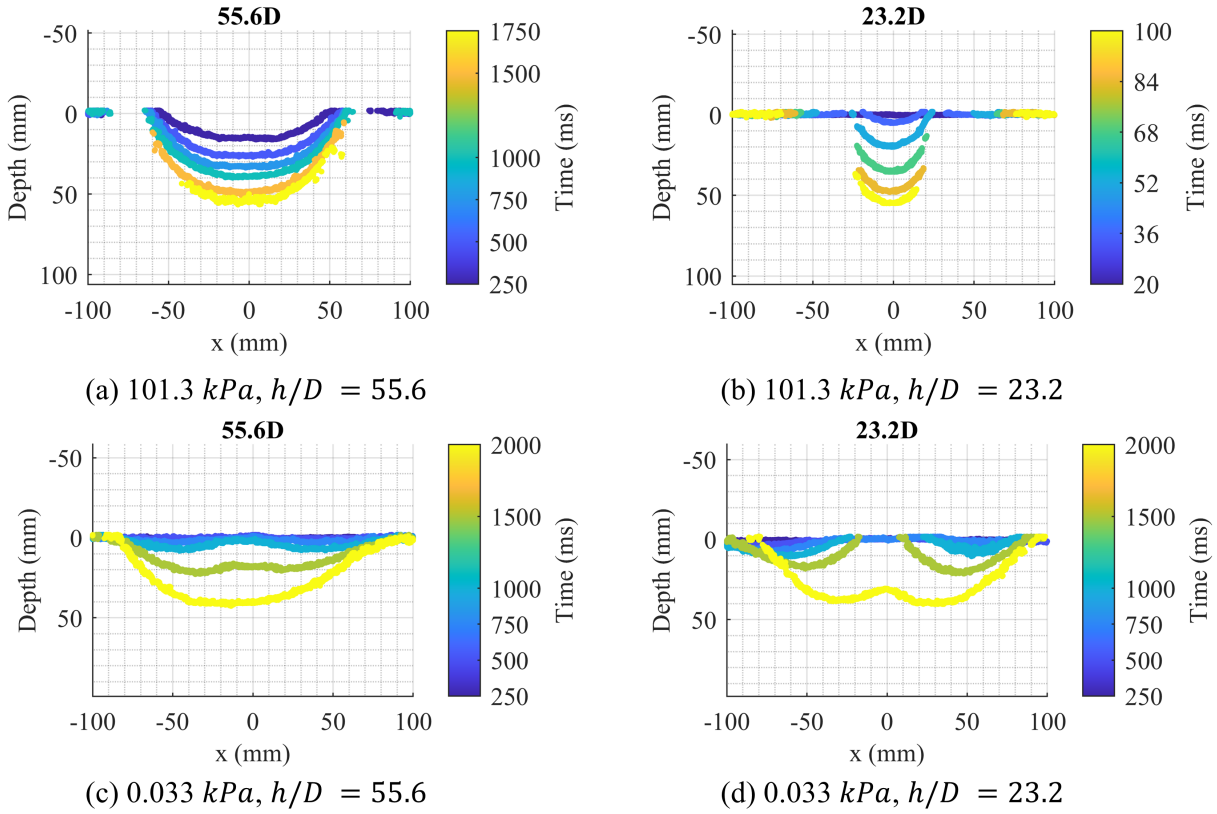

Figure 5: Cross-sectional view of the crater evolution over time for two nozzle heights and ambient pressure conditions tested. Color denotes time progression, and the specific time steps shown in each case are the labels on the color bar

observed in recent studies by Rubio et al. [35], Stubbs [32], and Balakrishnan et al. [36], but the physics driving the geometry of the lobed crater has not been identified. These observations clearly highlight the influence of nozzle height and ambient pressure conditions on the cratering dynamics.

These changes in the cratering dynamics also significantly influence the ejecta behavior. When the nozzle height is reduced from $h/D = 37.1$ to $h/D = 9.3$ (refer to Fig. 6), the ejecta's ejection angle increases, corresponding to an increase in the crater ramp angle. At higher nozzle heights, the ejecta travels at shallow angles away from the nozzle. However, at lower nozzle heights, the ejecta is directed vertically upward toward the nozzle, even during the initial phase of the jet impinging on the sand surface. Similarly, the ejection angle is considerably shallower under rarefied conditions than under continuum conditions. Although the ejection angle increases with time under rarefied conditions, it remains significantly smaller than observed under continuum conditions. This aligns with the presence of a shallower crater under rarefied conditions compared to the continuum cases. These observations suggest that the properties of the ejecta depend on the changes in the crater shape induced by the operating conditions of the nozzle. The following sections present the changes in ejecta kinematics under different ambient pressure conditions and nozzle heights and discuss the dependence on the crater shape and nozzle properties.

Ejecta trajectories and kinematics

Ejecta trajectories

From the particle tracking velocimetry measurements, the ejecta were tracked over a length much shorter than their full trajectory because of obfuscation from the out-of-plane ejecta. As such, a ballistic model was used to estimate and study the full ejecta trajectory. Ejecta with Stokes number $St_k \ll 1$ is expected to follow the flow, whereas ejecta with $St_k \gg 1$ has a motion independent of the surrounding flow field. The Stokes number for the mean size of the

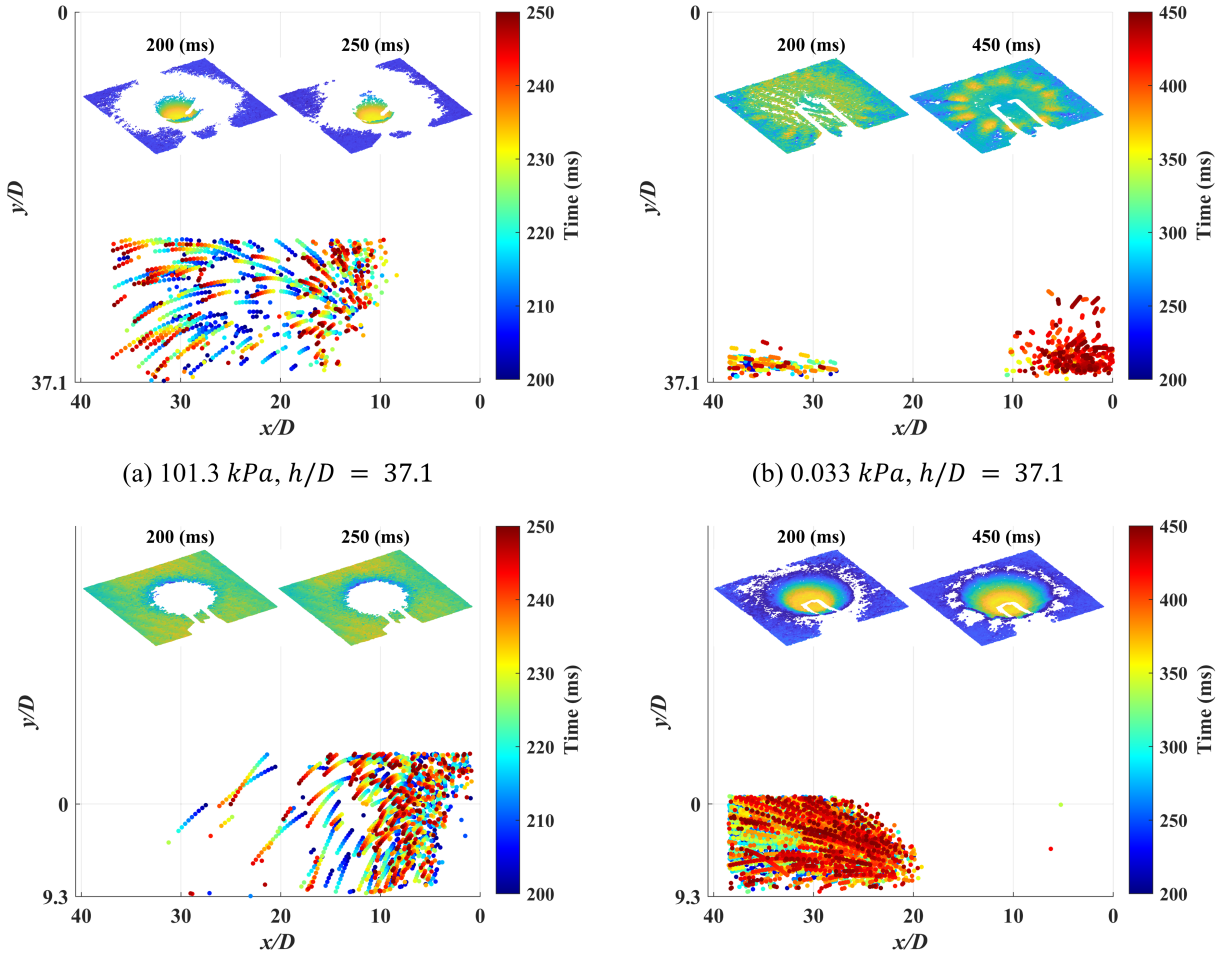

(a) 101.3 kPa, $h/D = 37.1$

(b) 0.033 kPa, $h/D = 37.1$

(c) 101.3 kPa, $h/D = 9.3$

(d) 0.033 kPa, $h/D = 9.3$

Figure 6: Measured ejecta trajectories and crater reconstructions for (a) h/D = 37.1 at 101.3 kPa, (b) h/D = 37.1 at 0.033 kPa, (c) h/D = 9.3 at 101.3 kPa, and (d) h/D = 9.3 at 0.033 kPa. The origin (0,0) in the figure indicates the nozzle exit center.

ejecta and the range of velocities is $St_k \approx 5500$, which implies that the ejecta would follow a ballistic path given an initial momentum impulse.

In addition, a statistical approach was adopted to further verify the validity of using the ballistic model and to determine if there is any influence of high-speed flow from the jet that could alter the ballistic path of this ejecta. The difference between the measured tracks (red dots in Fig. 7) and ballistic tracks (black dashed lines in Fig. 7) was quantified by computing the root mean square error (RMSE) during the time period for which the measured tracks were visible ($t_1 - t_2$). Here, it is important to note that the identified paths for different ejecta covered various stages of the ballistic trajectory (Fig. 7), providing comprehensive coverage of the full range of ejecta behavior over the duration of the tests. The mean and median RMSE was less than $0.1D$ (0.49 mm) for the range of parameter space in this study (as shown in Fig. 8). This has a significant implication since the ballistic model could be used to estimate (via extrapolation) the initial conditions of ejection near the crater rim location where the illumination is limited due to shadows cast by the ejected particles. Similarly, a first-order estimate of the maximum range and height of the ejecta can also be extracted, even though the field of view was limited.

While extracting properties such as the maximum ejecta range and heights, air drag could influence the ejecta movement, especially for continuum cases during the later stages of its ballistic path where the ejecta has reduced velocities. This could induce an error in the estimation of the ejecta range and height from the ballistic model. As such, the drag length (L_{drag}) was calculated to quantify the distance over which the air drag has appreciable effect on

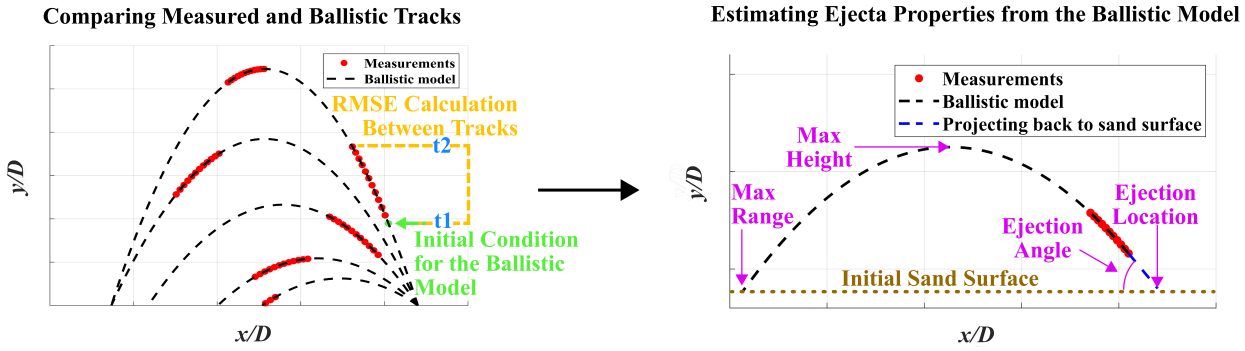

Figure 7: Summary of the implementation of the ballistic model to analyze the current results

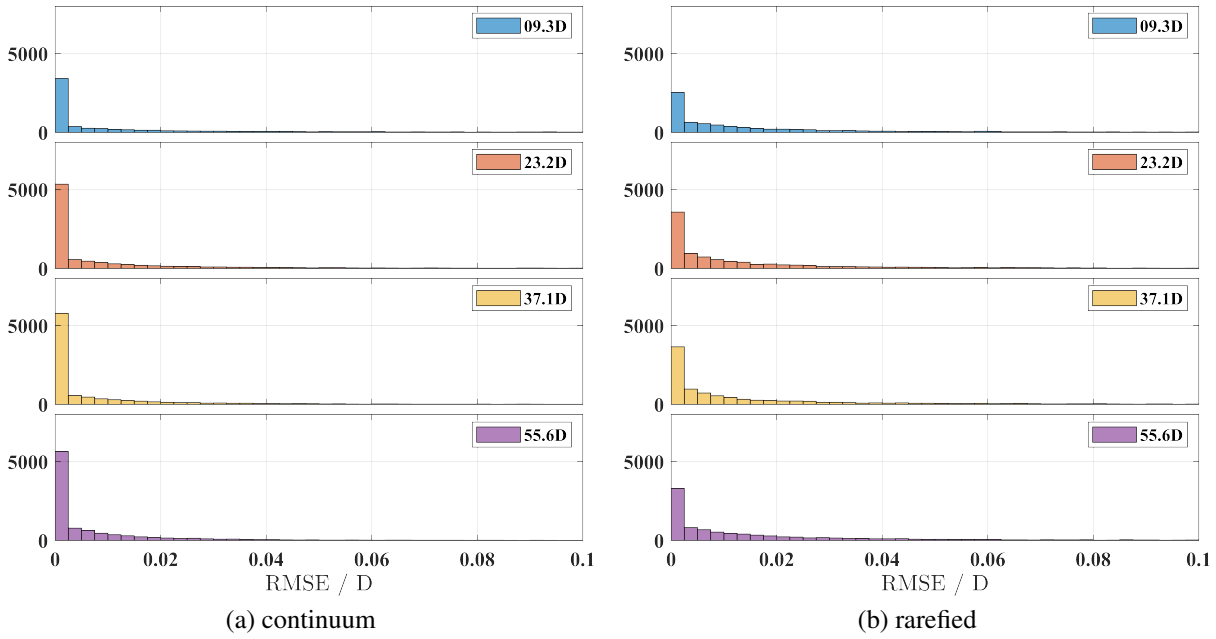

Figure 8: Root mean square error (RMSE) between the measured ejecta and ballistic tracks across several nozzle heights and ambient pressure conditions.

the movement of the ejecta [37]. The drag length is given as:

$$L_{drag} = \frac{4 d_p \rho_p}{6 \rho_{air}} \tag{4}$$

The drag length for the current mean particle size was calculated to be $L_{drag} \approx 0.9m$, which is greater than the distance traveled under continuum conditions by the ejecta in this study. As such, it can be safely assumed that air drag does not have any appreciable influence on current estimates from the ballistic model.

Ejecta kinematics

Ejecta velocity: Figure 9(a) shows the time evolution of ejecta velocity magnitude at the undisturbed sand surface for chamber pressure conditions of $101.3kPa$ (red) and $0.033kPa$ (black) at several nozzle heights. Under continuum conditions, the ejecta velocity at a higher nozzle height of $h/D = 55.6$ starts at a large value of nearly $5m/s$ and gradually decreases over time. At lower nozzle heights under continuum conditions, the magnitude of ejecta velocity

exhibits an initial sharp increase due to the impulse generated by the jet upon its initiation, which was not observed for higher nozzle heights. This velocity rapidly decreases and stabilizes at values around $1m/s$. In particular, the peak impulse velocity is highest for the nozzle height of $h/D = 37.1$, while consistently lower values are observed for lower nozzle heights of $h/D = 23.2$ and 9.3, despite maintaining a constant total nozzle pressure in these cases.

Under rarefied pressure conditions of $33Pa$, Stubbs et al. [32] reported that at the high nozzle height of $h/D = 55.6$, the crater does not develop until around $500ms$ after jet initiation. The magnitude of velocity measured at the same conditions also indicates slow-moving ejecta $\leq 1m/s$. Beyond $500ms$, ejecta velocity magnitude rises steeply to $5m/s$. Under rarefied conditions, when the nozzle height is reduced, the crater begins to form much earlier than $500ms$ as opposed to larger nozzle heights. Consequently, the magnitude of the velocity of the ejecta began to increase earlier and reached peak values of approximately $5.5m/s$. Overall, the magnitude of ejecta velocity was consistently greater under rarefied conditions compared to the continuum cases.

This could be due to several factors. One of the important factors could be the flow structure formed during the impingement of the under-expanded jet. The flow structure can be divided into a free jet, an impingement zone, and a wall jet. The reader is referred to the previous literature for a detailed understanding of the under-expanded jet impinging on a surface [38, 39]. Here, the impingement area is characterized by high stagnation pressure and the formation of a stagnation bubble. Meanwhile, the flow in the wall jet experiences rapid acceleration under rarefied conditions. These high velocities in the wall jet region could impart higher ejection velocities under rarefied conditions. Another factor that could be important is the breakdown of the no-slip boundary condition at these rarefied conditions [40], and thus the particles on the surface experience a higher drag. The combination of these factors could result in the particles attaining higher velocities under the low ambient pressure conditions currently tested.

The temporal evolution of ejecta velocities exhibited non-linear changes, unlike continuum cases where ejecta velocity gradually stabilized to a steady value after the initial impulse. These non-linear variations can be attributed to changes in chamber pressure during the test duration. The chamber pressure gradually increases from the initial value of $33Pa$ as the nozzle continues to operate, leading to a gradual jet contraction, as illustrated in Fig 4. These dynamic changes in jet behavior likely contribute to the observed non-linear variations in the ejecta behavior. It is crucial to note that significant changes in jet behavior occur after approximately $1000ms$, suggesting minimal effects on ejecta behavior before this time. These results underscore the challenges of maintaining rarefied conditions in current small-scale vacuum chambers while the nozzle is in operation. For a more in-depth understanding of PSI under rarefied conditions, further studies are necessary to isolate the effects of rarefied conditions from dynamic changes in jet behavior.

Ejection angle: Figure 9(b) shows the time evolution of ejection angle. Under continuum conditions, the ejection angle (from horizontal) at a higher nozzle height of $h/D = 55.6$ shows a monotonic increase over time. In contrast, the ejection angle at lower nozzle heights of $h/D = 37.1, 23.2, 9.3$ under continuum conditions experiences a rapid increase over time, up to 90°. Under rarefied conditions, ejection angles at $h/D = 55.6$ experience a gradual rise to 60°, which falls to approximately 10°. Beyond $500ms$, the shallow ejection angle gradually increases with time. Furthermore, the ejection angles observed at these nozzle heights of $h/D = 55.6, 37.1, 23.2, 9.3$ under rarefied conditions were significantly lower compared to the continuum cases.

Ejecta trajectory height and range: Under continuum case for the nozzle height of $h/D = 55.6$, the trajectory height H rises to $40D$ until $500ms$ as seen in Fig. 9(c) which is associated with the rise in ejection angle observed in Fig. 9(b). After this time, the ejecta trajectory height starts decreasing primarily due to the reduction in ejecta velocity magnitude. Ejecta trajectory range R (Fig. 9(d)) also follows a similar trend as height H and achieves a peak value of about $100D$. At lower nozzle heights under the continuum case, the ejecta trajectory height (H) initially exceeds the nozzle height itself (as indicated by the horizontal dotted line in Fig. 9(c)) during the initial impact phase. As time progresses, the ejecta trajectory height H settles down to values close to the nozzle height h. Finally, the ejecta trajectory range R seen in Fig. 9(d) is significantly lower at lower nozzle heights primarily due to the steep ejection angles close to 90°.

In rarefied cases, the ejecta trajectory heights were generally lower than those observed under continuum conditions and did not exceed the corresponding nozzle heights during the initial phases (up to $1000ms$), primarily due to the shallow ejection angle. However, as the ejection angles became steeper, the heights of the ejecta trajectory gradually exceeded the height of the nozzle h. Additionally, the shallower ejection angles under rarefied conditions resulted in a generally larger ejecta trajectory range than under continuum conditions.

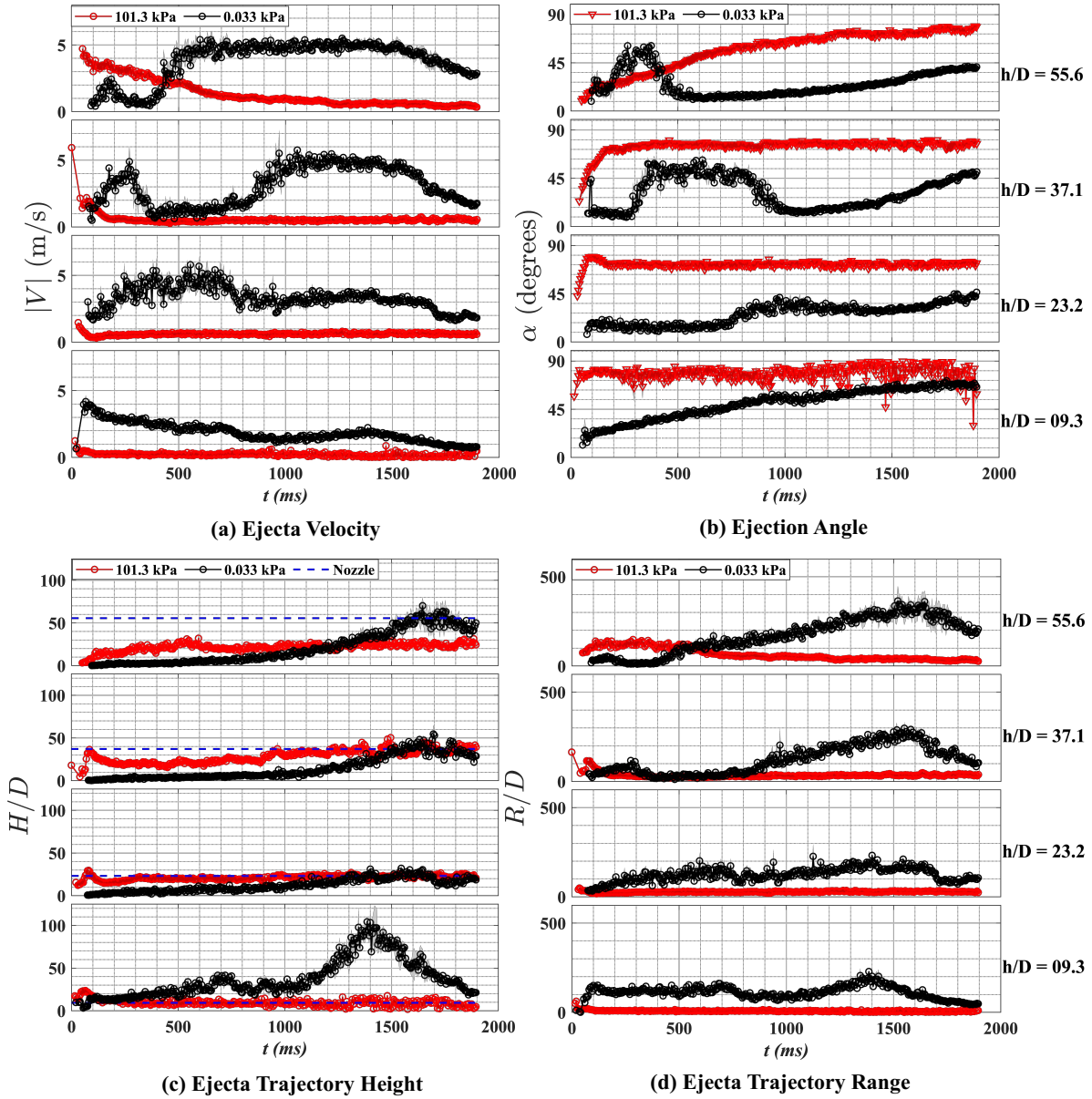

Figure 9: Temporal evolution of ejecta velocity magnitude, ejection angle, height, and range under continuum and rarefied conditions.

Correlation between ejecta kinematics and crater topology

The ejecta kinematics depend on the initial conditions, such as the initial location and angle of ejection. Identifying these properties can assist with augmenting the physical understanding of the PSI process in rarefied conditions. As such, the location and angle of the ejection were quantified for each condition and compared with the properties of the crater to develop any correlation between the crater shape and the ejecta behavior.

Crater rim and ejection location

The crater rim location was extracted from stereo measurements, and the ejection location was determined using the ballistic model's projection. The results for nozzle heights of $h/D = 55.6, 37.1, 23.2$, and 9.3 are shown in Fig. 10. The crater was not well-defined in the initial stages, and the crater rim location is set to zero. Despite the underdeveloped crater, the particle ejection locations seem to be concentrated at a finite distance from the nozzle

center. This distance likely corresponds to the initial impingement area of the jet on the sand surface. During the initial stages, high variation in the ejection location was observed, possibly due to the absence of a well-defined crater. In this phase, particles experience an initial upliftment from the surface due to the jet's impact, followed by an entrainment in the fluid with different initial ejection properties based on local radial fluid flow. These phenomena could also result in higher ejecta velocities during the initial stages discussed in the previous section. Further research is needed to explore these phenomena.

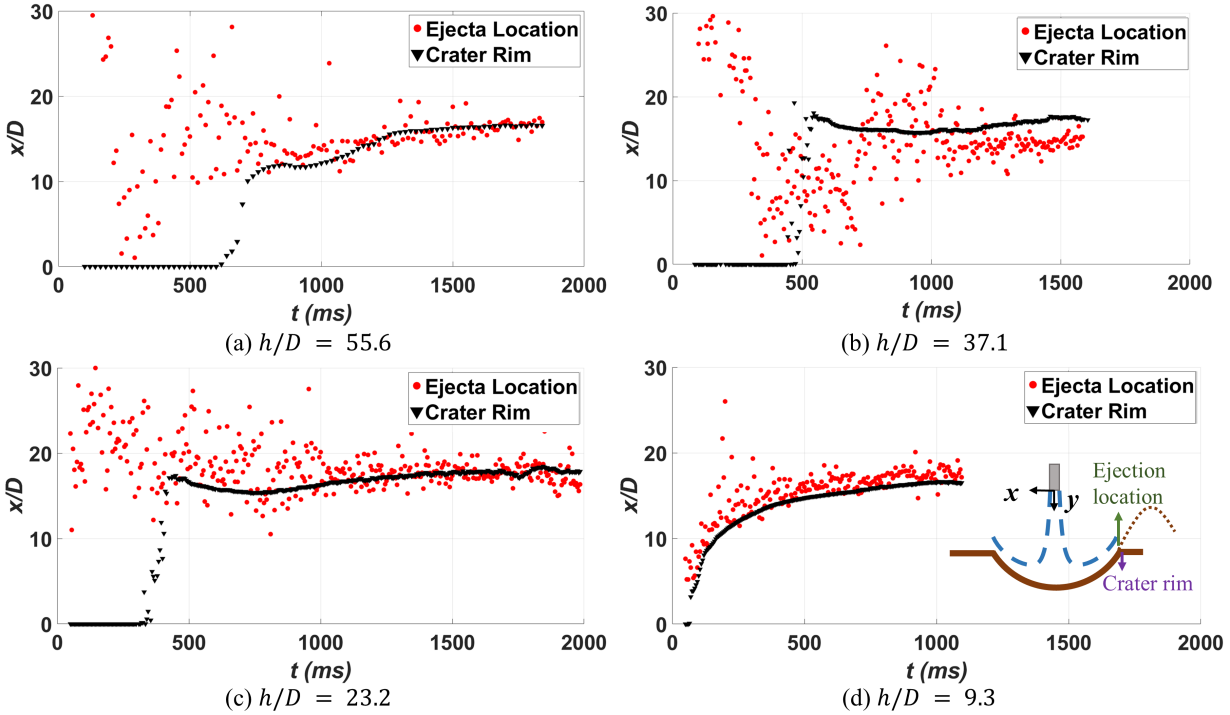

(a) $h/D = 55.6$ (b) $h/D = 37.1$

(c) $h/D = 23.2$ (d) $h/D = 9.3$

Figure 10: Crater rim location and the ejecta location for different nozzle heights at 0.033 *kPa* ambient pressure. The inset schematic illustrates the crater rim location and ejecta ejection location.

The ejection location centers around the crater rim as the crater shape evolves. The variance in the ejection location observed during the initial stages is reduced. Most particles now appear to be ejected from the crater rim location. This is likely due to the crater redirecting the flow at an angle corresponding to the crater wall angle. During this period, the shear and drag forces from the fluid on the simulant bed could transport particles from the crater to the crater rim, where they are ejected at a specific velocity corresponding to the shear and drag forces. An interesting observation is that there was still some variation in the ejection location even when the crater shape was well-developed. These could have resulted from occasional collisions between the particles that could have derailed the trajectories of these ejecta. These observations were mostly true for all nozzle heights tested.

Table 2: Summary of correlation analysis between crater wall and ejection angles.

h/D	Temporal range	Slope (m)	Intercept (c)	R^2	$p-value$
55.6	(700-1850) *ms*	0.63	10.07	0.9	≤ 0.05
37.1	(900-1500) *ms*	0.9	11.2	0.81	
23.2	(500-1500) *ms*	0.71	10.24	0.82	
9.3	(400-800) *ms*	0.85	14.5	0.77	

Crater ramp angle and ejection angle

Robert's analytical formulation [8, 10] developed during the Apollo era predicted that the ejection angle primarily depends on the crater's ramp angle. For the current experiments, the crater was observed to get deeper and the angle of the crater ramp increased with increasing time. At the same time, the ejection angle also increased with increasing time. The current analysis focuses on quantifying if the current changes in the ejection angle are primarily dependent on the crater ramp angle, as predicted by Robert's theory. For this quantification, a linear regression model was used. The linear regression model for all the nozzle heights of $h/D = 55.6, 37.1, 23.2$ & 9.3 has been shown in Fig. 11.

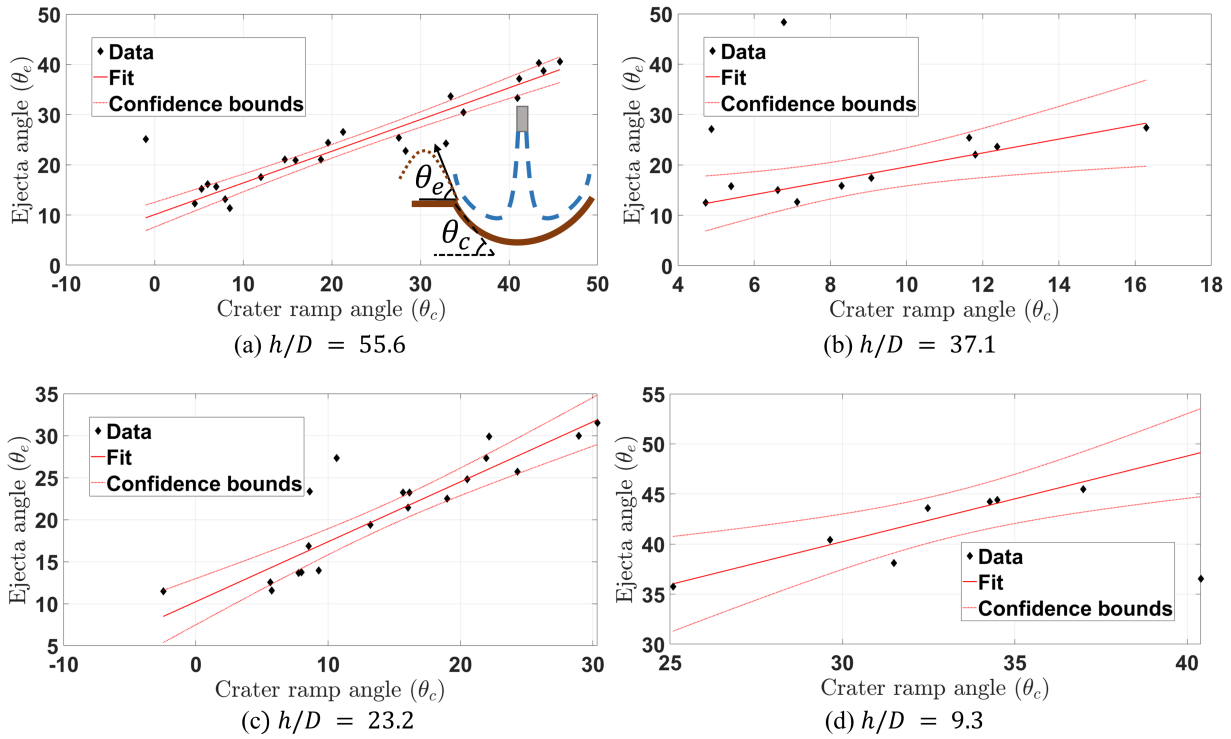

Figure 11: Linear regression model for different nozzle heights at 0.033 kPa ambient pressure ($R^2 \geq 0.7$, $p \leq 0.05$). The inset schematic illustrates the crater ramp angle and the ejection angle.

The summary of the slope and intercept of the linear regression model, coefficient of determination (R^2), and the correlation significance ($p - value$) for the ANOVA test are provided in Table 2. In all cases, an $R^2 \geq 0.77$ was observed, and the ANOVA test showed that the correlation between the crater ramp angle and ejecta angle was statistically significant ($p \leq 0.05$). The residual between the predicted value and the population (r_θ) in the time range specified in Table 2 was then calculated for all measurements at each nozzle height. The results are summarized in Fig. 11. The residuals were observed to be normally distributed and centered around zero. The current analysis shows a statistically significant correlation between the crater ramp angle and the ejection angles.

The findings indicate that the temporal changes in the ejection angle are strongly influenced by variations in the crater ramp angle under current test conditions. The observed alterations in the crater ramp angle, particularly beyond 1000 ms, can be linked to shifts in jet dynamics induced by the rise in chamber pressure. Despite these dynamics, the ejection angle values directly reflect changes in the crater ramp. This aligns with Roberts' predictions; however, recent research suggests that the ejection angle depends not only on the crater ramp angle but also on jet flow properties. Immer's [41] analysis of Apollo Lunar Module landing videos revealed that ejection angles changed with alterations in engine thrust. He posited that the crater shape remains relatively constant during the temporal scales of ejection angle changes. In the current experiments, the flow conditions of the nozzles were kept constant by maintaining total pressure throughout the test. Any changes in flow as a result of the increase in pressure were gradual. Without transient events like thrust modulation, it seems that the ejection angle is predominantly influenced by the crater ramp

angle. Further research is needed to quantify the impact of transient changes in the operating conditions of the nozzle.

Discussion

The results reveal notable distinctions in cratering and ejecta dynamics under rarefied atmospheric conditions compared to continuum conditions. Craters formed under rarified conditions are significantly shallower and wider, displaying lobed features absent in Earth's atmospheric conditions. The shallower craters result from a larger impingement area due to under-expansion of the jet in rarefied conditions. The dominant erosion mechanism observed under these rarefied conditions is viscous erosion, evident from the maximum depth that occurs radially outwards from the nozzle axis. Ejection velocities are notably higher under rarefied conditions, attributed to flow acceleration and the breakdown of the no-slip boundary conditions. The ejection angle is influenced by changes in the shape of the crater, particularly in the presence of a well-defined crater. An increase in the ejection angle correlates with an increase in the crater ramp angle, and the ejection location is concentrated around the crater rim. The ejection angle is lower under rarefied conditions, likely due to the formation of a shallower crater.

The findings offer preludes to the potential effects during PSI under rarefied atmospheric conditions, as encountered on celestial bodies such as the Moon and Mars. The jet impinging on the simulant surface is highly underexpanded, resulting in wider and shallower craters, aligning with previous literature [8]. Expectations include higher ejection velocities and much shallower ejection angles under these rarefied conditions. Furthermore, the formed craters may exhibit lobed structures, though further research is needed to explore this phenomenon. Certainly, future investigations should extend their focus to factors not currently considered. In lunar and Martian conditions, the jet impinging on the regolith consists of hot gases, differing from the cold flow conditions studied here. This alteration in flow features due to hot exhaust might yield different results. For example, a recent numerical study has shown that jets with a lower stagnation temperature impart a higher normal pressure, whereas jets with a higher stagnation temperature impart a higher shear stress on the impinging surface [42]. These effects can result in varying local flow properties that modify the shape of the crater and the ejection properties.

Furthermore, the effects of cohesive and gravitational forces also need to be considered. A recent study showed that a simulant surface with tri-dispersed simulant showed a lower erosion rate compared to a mono-dispersed simulant bed with larger particle sizes [28]. These results were attributed to the low porosity and high friction between the particles in the tri-dispersed simulant bed. Similarly, previous studies have shown that the effects of PSI are more severe under reduced gravity conditions, likely due to the reduction in the body forces that oppose the forces imparted by the jet [43, 44]. While some current observations might still be valid when these additional effects are considered, a comprehensive understanding demands the exploration of these factors through additional experiments with a broader parametric space. The high-fidelity quantitative measurement techniques adopted in this study offer a viable path to further understanding PSI under relevant conditions. Subsequent studies should particularly emphasize the consideration of additional parameters discussed above.

4. Conclusion

The current work focuses on studying the effects of nozzle heights and ambient pressure conditions on ejecta dynamics during plume-surface interactions. The nozzle heights were varied as $h/D = 55.6, 37.1, 23.2$ & 9.3, and the ambient pressure condition was varied as $101.3\ kPa$ and $0.033\ kPa$. Two-dimensional particle tracking velocimetry was used to quantify the ejecta kinematics. Simultaneous crater measurements were also performed using stereo photogrammetry to quantify the influence of the crater on the ejecta behavior. Some of the conclusions that can be drawn from this study are summarized below.

1. The ejecta experienced the largest velocities during the initial jet impact phase under continuum conditions. For the rarefied cases, the effects of initial impact of the jet were only apparent for the lowest nozzle height of $h/D = 9.3$.
2. Ejection angles were lower and velocities were higher in rarefied atmospheric cases compared to continuum atmospheric cases. Consequently, the ejecta traveled farther in the rarefied case, while vertically higher in the continuum case.

3. Quantification of the location of the crater rim from the stereo photogrammetry measurements and the location of ejection from the particle tracking velocimetry measurements showed that most of the ejecta were ejected from the crater rim, especially when a well-defined crater was present.
4. For the current conditions tested, the changes in the ejection angle correlated well with the changes in the crater ramp angle.

5. Acknowledgements

The authors would like to thank Dr. Ashley Korzun at NASA Langley Research Center, Dr. Wesley Chambers at NASA Marshall Space Flight Center, and Dr. James Mantovani from Kennedy Space Center for their valuable feedback and discussions during this work. The authors also acknowledge the assistance of the members of the Auburn University Combustion Physics Laboratory, the Applied Fluids Research Group, and the Advanced Flow Diagnostics Laboratory. This work was completed in part with resources provided by the Auburn University Easley Cluster. The assistance of Mr. Andy Weldon in the fabrication of the experimental setup is gratefully acknowledged.
Funding: This work was supported by an Early Stage Innovations (ESI) grant from NASA's Space Technology Research Grants Program - Grant Number 80NSSC20K0300 (Technical Point of Contact - Dr. James G Mantovani). BF and VR acknowledge partial support from the National Science Foundation under Grant number 2035488, monitored by Dr. Ronald Joslin.

References

[1] A. Rahimi, O. Ejtehadi, K. Lee, R. Myong, Near-field plume-surface interaction and regolith erosion and dispersal during the lunar landing, Acta Astronautica 175 (2020) 308–326. doi:https://doi.org/10.1016/j.actaastro.2020.05.042.
[2] C. Immer, P. Metzger, P. E. Hintze, A. Nick, R. Horan, Apollo 12 lunar module exhaust plume impingement on lunar surveyor iii, Icarus 211 (2) (2011) 1089–1102. doi:10.1016/j.icarus.2010.11.013.
[3] J. R. Gaier, The effects of lunar dust on eva systems during the apollo missions, Tech. Rep. TM—2005-213610/REV1, NASA (2007).
[4] A. B. Morris, D. B. Goldstein, P. L. Varghese, L. M. Trafton, Approach for modeling rocket plume impingement and dust dispersal on the moon, Journal of Spacecraft and Rockets 52 (2) (2015) 362–374. doi:10.2514/1.A33058.
[5] W. Carroll, P. Blair Jr, Lunar dust and radiation darkening of surveyor 3 surfaces, analysis of surveyor 3 materials and photographs returned by apollo 12, NASA SP-284 (1972) 158–167.
[6] P. T. Metzger, J. Smith, J. E. Lane, Phenomenology of soil erosion due to rocket exhaust on the moon and the mauna kea lunar test site, Journal of Geophysical Research: Planets 116 (E6) (2011). doi:10.1029/2010JE003745.
[7] P. Prem, D. M. Hurley, D. B. Goldstein, P. L. Varghese, The evolution of a spacecraft-generated lunar exosphere, Journal of Geophysical Research: Planets 125 (8) (2020) e2020JE006464.
[8] L. Roberts, The action of a hypersonic jet on a dust layer, in: Institute of Aerospace Sciences 31st Annual Meeting, 1963.
[9] L. Roberts, Visibility and dust erosion during the lunar landing, A compilation of recent research related to the Apollo Mission (1963) 155–170.
[10] L. Roberts, Exhaust jet — dust layer interaction during a lunar landing, in: XIIIth International Astronautical Congress Varna 1962, Springer, 1964, pp. 21–37. doi:10.1007/978-3-7091-4688-0_3.
[11] L. Roberts, The interaction of a rocket exhaust with the lunar surface (rocket exhaust jet interaction with lunar surface dust layer), Agard the Fluid Dyn. Aspects of space flight 2 (1966).
[12] NASA, Four Out of Six Apollos (2008).
[13] R. E. Hutton, Comparison of soil erosion theory with scaled lm jet erosion tests, Tech. Rep. CR-66704, NASA (1968).
[14] J. Alexander, W. Roberds, R. Scott, Soil erosion by landing rockets, Tech. Rep. CR-65484, NASA (1966).
[15] R. F. Scott, H.-Y. Ko, Transient rocket-engine gas flow in soil., AIAA Journal 6 (2) (1968) 258–264. doi:10.2514/3.4487.
[16] P. T. Metzger, J. E. Lane, C. D. Immer, S. Clements, Cratering and blowing soil by rocket engines during lunar landings, in: International Conference on Case Histories in Geotechnical Engineering, 2008.
[17] P. T. Metzger, C. D. Immer, C. M. Donahue, B. T. Vu, R. C. Latta, M. Deyo-Svendsen, Jet-induced cratering of a granular surface with application to lunar spaceports, Journal of Aerospace Engineering 22 (1) (2009) 24–32. doi:10.1061/(ASCE)0893-1321(2009)22:1(24).
[18] R. B. Haehnel, B. Cushman-Roisin, W. B. Dade, Cratering by a subsonic jet impinging on a bed of loose particles, in: Earth & Space 2006, 2006, pp. 1–8. doi:10.1061/40830(188)19.
[19] R. B. Haehnel, W. B. Dade, B. Cushman-Roisin, Crater evolution due to a jet impinging on a bed of loose particles, in: Earth & Space 2008, 2008, pp. 1–10. doi:10.1061/40988(323)2.
[20] C. Immer, P. Metzger, Rocket cratering in simulated lunar and martian environments, in: Earth and Space 2010: Engineering, Science, Construction, and Operations in Challenging Environments, 2010, pp. 182–190. doi:10.1061/41096(366)20.
[21] S. D. Guleria, D. V. Patil, Experimental investigations of crater formation on granular bed subjected to an air-jet impingement, Physics of Fluids 32 (5) (2020) 053309. doi:10.1063/5.0006613.
[22] C. Q. LaMarche, J. S. Curtis, P. T. Metzger, Cratering of a lunar soil simulant, jsc-1a, by a turbulent subsonic jet, in: Earth and Space 2012: Engineering, Science, Construction, and Operations in Challenging Environments, 2012, pp. 36–44. doi:10.1061/9780784412190.005.

[23] C. Q. LaMarche, J. S. Curtis, Cratering of a particle bed by a subsonic turbulent jet: Effect of particle shape, size and density, Chemical Engineering Science 138 (2015) 432–445. doi:10.1016/j.ces.2015.08.030.
[24] P. T. Metzger, R. C. Latta, J. M. Schuler, C. D. Immer, Craters formed in granular beds by impinging jets of gas, in: AIP Conference Proceedings, Vol. 1145, 2009, pp. 767–770. doi:10.1063/1.3180041.
[25] M. Mehta, A. Sengupta, M. Pokora, L. Hall, N. Renno, Mars landing engine plume impingement ground interaction, in: Earth and Space 2010: Engineering, Science, Construction, and Operations in Challenging Environments, 2010, pp. 143–157. doi:10.1061/41096(366)17.
[26] C. J. Eberhart, J. West, A. M. Korzun, Overview of plume-surface interaction data from subscale inert gas testing at nasa msfc test stand 300 vacuum facilities, in: AIAA Scitech 2022 Forum, 2022, p. 1811.
[27] D. C. Stubbs, L. Silwal, B. S. Thurow, M. Hirabayashi, V. Raghav, D. E. Scarborough, Three-dimensional measurement of the crater formation during plume–surface interactions using stereo-photogrammetry, AIAA Journal 60 (3) (2022) 1316–1331.
[28] J. S. Rubio, M. Gorman, M. X. Diaz-Lopez, R. Ni, Plume-surface interaction physics focused ground test 1: Setup and preliminary results, in: AIAA SCITECH 2022 Forum, 2022, p. 1809.
[29] M. X. Diaz-Lopez, M. Gorman, J. S. Rubio, R. Ni, Plume-surface interaction physics focused ground test 1: Diagnostics and preliminary results, in: AIAA Scitech 2022 Forum, 2022, p. 1810.
[30] A. Kaehler, G. Bradski, Learning OpenCV 3: Computer Vision in C++ with the OpenCV Library, O'Reilly Media, 2016.
[31] P. Burdziakowski, UAV Design and Construction for Real Time Photogrammetry and Visual Navigation, in: Proceedings - 2018 Baltic Geodetic Congress, BGC-Geomatics 2018, Institute of Electrical and Electronics Engineers Inc., 2018, pp. 368–372. doi:10.1109/BGC-Geomatics.2018.00076.
[32] D. Stubbs, L. Silwal, V. N. Bhargav, B. S. Thurow, M. Hirabayashi, V. Raghav, D. E. Scarborough, Non-intrusive, 3-d crater formation measurements due to plume-surface interactions under sub-atmospheric pressure conditions, in: AIAA SCITECH 2023 Forum, 2023, p. 2488.
[33] J. Schindelin, I. Arganda-Carreras, E. Frise, V. Kaynig, M. Longair, T. Pietzsch, S. Preibisch, C. Rueden, S. Saalfeld, B. Schmid, et al., Fiji: an open-source platform for biological-image analysis, Nature methods 9 (7) (2012) 676–682.
[34] D. B. Allan, T. Caswell, N. C. Keim, C. M. van der Wel, R. W. Verweij, soft-matter/trackpy: v0.6.1 (Feb. 2023). doi:10.5281/zenodo.7670439.
[35] J. S. Rubio, M. Gorman, M. X. Diaz-Lopez, R. Ni, Plume-Surface Interaction Physics Focused Ground Test 1: Setup and Preliminary Results, AIAA Science and Technology Forum and Exposition, AIAA SciTech Forum 2022 (2022). doi:10.2514/6.2022-1809.
[36] K. Balakrishnan, J. Bellan, High-fidelity modeling and numerical simulation of cratering induced by the interaction of a supersonic jet with a granular bed of solid particles, International Journal of Multiphase Flow 99 (2018). doi:10.1016/J.IJMULTIPHASEFLOW.2017.08.008.
[37] W. K. Hartmann, Impact experiments: 1. ejecta velocity distributions and related results from regolith targets, Icarus 63 (1) (1985) 69–98.
[38] P. Lamont, B. Hunt, The impingement of underexpanded, axisymmetric jets on perpendicular and inclined flat plates, Journal of Fluid Mechanics 100 (3) (1980) 471–511.
[39] M. Mehta, N. O. Renno, J. Marshall, M. Rob Grover, A. Sengupta, N. A. Rusche, J. F. Kok, R. E. Arvidson, W. J. Markiewicz, M. T. Lemmon, P. H. Smith, Explosive erosion during the phoenix landing exposes subsurface water on mars, Icarus 211 (1) (2011) 172–194. doi:10.1016/j.icarus.2010.10.003.
[40] J. C. Maxwell, Vii. on stresses in rarified gases arising from inequalities of temperature, Philosophical Transactions of the royal society of London (170) (1879) 231–256.
[41] C. Immer, J. Lane, P. Metzger, S. Clements, Apollo video photogrammetry estimation of plume impingement effects, Icarus 214 (1) (2011) 46–52. doi:https://doi.org/10.1016/j.icarus.2011.04.018.
[42] M. B. Agir, C. White, K. Kontis, Impact of stagnation temperature and nozzle configuration on rarefied jet plume interactions, Journal of Spacecraft and Rockets 59 (5) (2022) 1536–1551.
[43] W. Chambers, A. Dove, C. Cox, P. Metzger, Plume-surface interaction phenomena observed in vacuum microgravity, in: Earth and Space 2021, 2021, pp. 22–31.
[44] T. Crane, D. Stubbs, B. S. Thurow, V. Raghav, D. Scarborough, Three-dimensional crater formation measurements during plume-surface interaction in a reduced gravity environment using a drop tower, in: AIAA SCITECH 2024 Forum, 2024, p. 2525.